Nuclear Engineering and Design 411 (2023) 112408

Contents lists available at ScienceDirect

Nuclear Engineering and Design

journal homepage: www.elsevier.com/locate/nucengdes

Importance, influence and limits of CFD radiation modeling for containment atmosphere simulations

Ralf Kapulla [a,*,1], Liu Xiongguo [b,1], Stephan Kelm [b], Ulrich Doll [a], Sidhart Paranjape [c,2], Domenico Paladino [a]

[a] Paul Scherrer Institute, Experimental Thermal-Hydraulics Group, Forschungstrasse 111, Villigen PSI, 5232, Switzerland
[b] Forschungszentrum Jülich GmbH, Institute for Energy and Climate Research (IEK-14), Wilhelm-Johnen-Straße, Jülich, 52428, Germany
[c] OST – Ostschweizer Fachhochschule, Departement Technik, Buchs, 9471, Switzerland

ARTICLE INFO

Keywords:
Containment flows
Gas radiation heat transfer
Non-gray gas radiation
Thermal radiation experiments
Gas compression
PANDA

ABSTRACT

In the appearance of steam, the CFD modeling of thermal-hydraulic phenomena in reactor containments during various phases of an accident necessarily requires consideration of radiative heat transfer. These radiation phenomena involve (i) energy transfer within the gas mixture and (ii) between the gas and the surrounding structures which have a much higher thermal inertia. Preliminary calculations performed for the present experiments in the OECD/NEA HYMERES-2 project with the CFD code *containmentFoam* using a Monte Carlo thermal radiation solver with non-gray gas modeling of steam absorption, showed that radiant heat transfer is important even with a very low amount of steam (≈ 2%). Therefore, the test matrix was tailored to the two opposite extremes: Either gas compositions with low steam content, where radiative heat transfer can be neglected, or gas mixtures containing larger amounts of steam, so that radiative heat transfer plays a dominant role. For the two selected experiments within the H2P2 series and the corresponding CFD calculations, a vessel with a diameter of 4 m and a height of 8 m was preconditioned with different mixtures of air/steam at room and elevated temperatures. This was followed by the build-up of a stable helium stratification in the upper part of the vessel. Helium was then injected from the top at a higher mass flow rate, which (a) compresses the gas atmosphere, (b) resembles piston compression and (c) leads to a height-dependent and transient increase in gas temperature below this helium stratification, influenced by thermal radiation effects — or their absence. These experiments and the associated CFD calculations were developed to isolate the thermal radiation phenomena as much as possible from convective and diffusive effects. They are the first of their kind to be conducted in a large-scale thermal-hydraulic facility. It is demonstrated (a) that neglecting thermal radiation for the high steam content case, the temperature rise is significantly over-predicted by a factor of two compared to the application of the suggested Monte Carlo thermal radiation solver with non-gray gas modeling, (b) the computational effort considering CFD and non-gray gas radiation is feasible with the suggested tailored Monte Carlo solver and (c) that the suggested radiation model outperforms the widespread used P1 radiation model.

1. Introduction

During postulated, (ERCOSAM, 2014), or real severe accidents, (Fujisawa et al., 2021; Skillman and Rempe, 2021; Sich, 2021; Steinhauser et al., 2014; Cilliers, 2013), large amounts of steam and hydrogen can be generated and released into the containment building, (Liu et al., 2021; Fujisawa et al., 2021; Ahmed et al., 2021; Saji, 2016). The mixing, distribution and transport of these gases are affected by thermal radiation (i) absorption and emission by non-gray gases (H_2O, CO_2 and CO) within the media and (ii) radiation transfer between the non-gray gas media and the dry and wetted containment structures, (Amend and Klein, 2020), which is due to the high absorption and emission of steam mainly in the infrared spectral range (Kapulla et al., 2022; Liu et al., 2022; Kapulla et al., 2021; Dehbi et al., 2019; Li et al., 2018; Kelm et al., 2016). Previous computational assessments of thermal-hydraulic experiments, like the TOSQAN 114 experiment conducted within the EURATOM-ROSATOM/ERCOSAM-SAMARA project, (Dabbene et al., 2015), provided initial insights into the potential impact of gas radiation heat transfer in the context of the total heat transport occurring in containment flows during an accident sequence (Filippov et al., 2016).

* Corresponding author.
E-mail address: ralf.kapulla@psi.ch (R. Kapulla).
[1] These authors have contributed equally to this article.
[2] Former PSI employee.

https://doi.org/10.1016/j.nucengdes.2023.112408
Received 14 October 2022; Received in revised form 23 May 2023; Accepted 23 May 2023
Available online 8 June 2023
0029-5493/© 2023 The Authors. Published by Elsevier B.V. This is an open access article under the CC BY-NC-ND license (http://creativecommons.org/licenses/by-nc-nd/4.0/).

Nomenclature

I_η	radiative intensity $Wm^{-2}sr^{-1}cm^{-1}$
$I_{b,\eta}$	emission radiative intensity $Wm^{-2}sr^{-1}cm^{-1}$
η	wavenumber cm^{-1}
ρ	density $kg\,m^{-3}$
$\mathbf{n}$	surface normal vector –
X_i	ith species mass fraction %
ν	kinematic viscosity $m^2\,s^{-1}$
τ	shear stress $kg\,m^{-1}\,s^{-2}$
Ω	solid angle sr
κ_η	absorption coefficient m^{-1}
ϵ	emissivity –, [0..1]
g	gravitational acceleration ms^{-2}
$\mathbf{r}$	position vector m
$\mathbf{U}$	velocity vector $m\,s^{-1}$
p	pressure $kg\,m^{-1}\,s^{-2}$
$-\nabla \cdot q_r$	radiative source term Wm^{-3}
q_r	radiative wall heat flux Wm^{-2}
t	time s
T	temperature K
E, A, D	phase indicators –
T_0	reference temperature K
T_w	weighted temperature K
T_e	excess temperature K
T_r	room temperature K
T_{el}	elevated temperature K
D	molecular diffusion coefficient ms^{-2}
h_{tot}	total enthalpy $kg\,m^2s^{-2}$
h_i	ith species total enthalpy $kg\,m^2s^{-2}$
Sc_t	(turbulent) Schmidt number –
k	turbulent kinetic energy m^2s^{-2}
ω	turbulence dissipation rate s^{-1}

Experiments such as performed in the medium-scaled THAI, (Vijaya Kumar et al., 2020), MISTRA, (NEA, 2012a) or TOSQAN facility, (Dabbene et al., 2015), as well as in the large-scale facility PANDA are preferred for these investigations, (Andreani et al., 2016; Visser et al., 2014), since experiments at smaller scale may suffer from inadequate scaling (Wang and Yan, 2021; Bestion, 2017). In addition, subsequent analysis of some previous PANDA experiments dealing with the erosion of a stratified containment atmosphere by a vertical jet has demonstrated the importance of thermal radiation in simulating the overall erosion process (Liu et al., 2022; Andreani et al., 2020, 2019; Dehbi et al., 2019; Kelm et al., 2016; Filippov et al., 2016).

Treatment of the spectral gas properties of gas mixtures containing infrared active gas molecules such as H_2O and CO_2 is not straightforward, (Vincenti and Traugott, 1971). Since steam exhibits high radiation absorption, especially in the infrared region, (Liu et al., 2022; Gordon et al., 2017), the strength of the thermal radiation in natural convection flows can compete with conduction and convection if (a) fluid velocities are comparatively low, (Vijaya Kumar et al., 2020), and (b) natural convection or low velocity flows are monitored over a long period of time (hours), (Dehbi et al., 2019). As a side note, in the context of infrared radiation phenomena, the magnitude of this time scale is similar important for the weather forecast and related phenomena (Cesari et al., 2022; Xu et al., 2022; Nielsen et al., 2021; Unterberger et al., 2021). Moreover, thermal radiation effects are related to absorption spectrum, fluid temperature, pressure and species partial pressures, (Modest, 2013). Therefore, computational modeling is still somewhat challenging in various fields of interest, (Liu et al., 2022; Piroozmand et al., 2020; Wang et al., 2014). Despite these difficulties, the numerical calculations and analyses performed within the Analytical Working Groups of the international PANDA projects (NEA, 2018, 2012a), taking into account the radiative heat transfer, have led to an improvement of the simulation results (Liu et al., 2022; Andreani et al., 2019; Filippov et al., 2016).

The effect of gas radiation on the temperature distribution within large free volumes is shown in Fig. 1 by example of the OECD/NEA SETH-2 ST1_1_2 experiment. These results were adopted from Liu et al. (2022). A hot steam jet was vertically injected into a colder environment with high steam content. Radiative heat transport promotes the heat transfer between the hot jet and media environment. This leads to an enhancement of the off-center temperature drop in the upper vessel region, similar to the gas temperatures recorded in the experiment. In contrast, neglecting the radiative heat transport results in a much higher prediction of the temperatures, Fig. 1(c).

Although radiative phenomena are implicitly included most of the time, previous test series in PANDA were not designed and performed with the *specific* aim of evaluating radiative heat transfer in large facilities, as has been done for other relevant components or phenomena, (Paladino and Dreier, 2012; Paladino et al., 2012). To address this gap, the H2P2 series of five tests represent the first PANDA experiments that were designed exclusively to improve the understanding of the importance of thermal radiation heat transfer in large free volumes under representative conditions derived from previous validation experiments and accident sequences (Kapulla et al., 2022). The test matrix was designed considering two bounding conditions: either a gas mixture with high steam concentrations where radiation heat transport impact can be significant (H2P2_5) or a nearly dry mixture with the lowest experimentally possible humidity where gas radiation is negligible (H2P2_1_2), (Kapulla et al., 2022). The comparison of these two experiments together with the corresponding results of CFD calculations is the subject of the present paper. Moreover, the computations including radiation effects will be contrasted with numerical simulations for H2P2_5 where radiative energy transport is neglected. The experiments of the H2P2 series were carried out in a single vessel of the PANDA facility, which significantly reduces the computational costs compared to other PANDA experiments that required modeling two interconnected vessels.

In the context of this work, it is important to note that some of the axis scales are not illustrated in the figures or are presented in relative values to prevent the release of the experimental data. The experimental data gained within the OECD/NEA HYMERES-2 project will be opened to the public in 2024. This paper aims to introduce the reader to the main phenomenology and characteristics of the test series and its phenomenology as well as first numerical insights from CFD simulations. For this purpose the article is structured in the following manner. Section 2 briefly summarizes the experiments conducted and the test matrix; a more in depth description can be found in Kapulla et al. (2022). In Section 3, the background of the CFD calculations, the implementation of the radiation framework used and details of the modeling strategy are given. The experimental and numerical results are evaluated in Section 4 with emphasis on the resulting temperature distributions and profiles in the compression and the subsequent decay period. The paper is summarized and conclusions are drawn in Section 5.

2. Experimental procedure

In this section, we give a brief description of the two experiments H2P2_1_2 and H2P2_5 considered for the present study, the initial and boundary conditions and the measurement accuracies. An overview of the entire series (five experiments) and a more detailed discussion can be found in Kapulla et al. (2022). The most important initial and boundary conditions for those two experiments are summarized in Table 1.

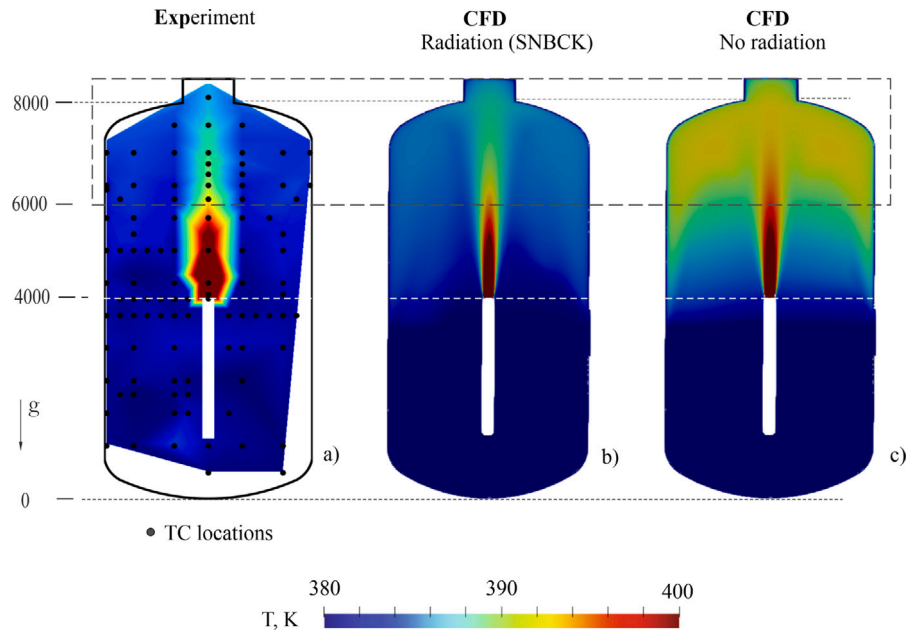

Fig. 1. Comparison of the temperature fields recorded for the experiment (a) and the corresponding numerical calculations considering radiation (b) or with neglected radiation (c). The presented experiment ST1_1_2 was conducted within the OECD/NEA SETH-2 project, (NEA, 2012a; Andreani et al., 2012), and the numerical results were adopted from Liu et al. (2022). Dimensions are in mm. The SNBCK model also used for the present CFD simulations is introduced in Section 3 with some details.

Table 1
Nominal conditions of experiments H2P2_1_2 and H2P2_5.

Experiment	→	H2P2_1_2[a]	H2P2_5[b]
Gas atmosphere	–	air	air
Initial temp.	–	T_r	T_{el}
Steam/Humidity	X_{st}%	**0.1**	**60**
Stratification	X_{He}%	50	50
He mass flow	g/s	10	10
Compression	s	1200	1200
Decay phase	s	>1200	>1200
Initial pressure	bar	1	1

[a]Reference experiment: Minimum experimentally achievable humidity.
[b]Highest initial humidity. Comparable to accident conditions.

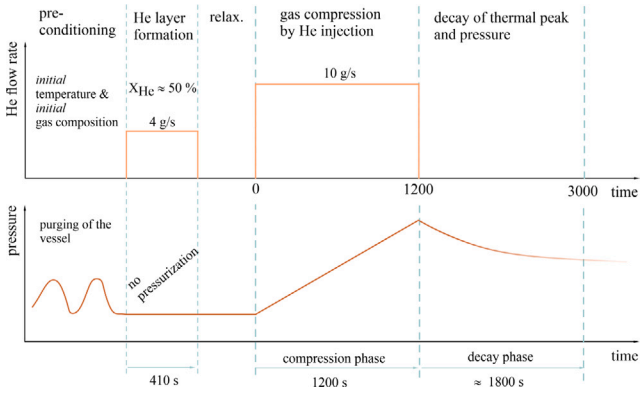

Fig. 2. Generalized test sequence for the H2P2 test series consisting in the pre-conditioning, the compression and the decay phase.

The experiment the H2P2_1_2 experiment was conducted starting from room temperature T_r. Its initial steam concentration was less than 0.1% to minimize the non-gray gas radiation within the medium. It is called the *reference case* in the following discussion. In contrary, the experiment H2P2_5 experiment was conducted at an elevated temperature level T_{el}, and at a high steam content around 60 vol.%, which is representative of accidental conditions. Under these conditions, non-gray gas radiation is considered to have a significant impact on the temperature field during the compression phase and the temperature decay subsequent to the stop of helium injection.

The generalized test sequence of the experiments is depicted in terms of the Helium injection rate and resulting pressure evolution in Fig. 2. A 3D rendering of the experimental setup within the single PANDA vessel for the H2P2 series (all units in mm) is given in Fig. 4. Prior to helium injection, the initial gas temperature and mixture composition were defined according to Table 1. The initial dry air for the H2P2_1_2 experiment by injecting dry air from the pressurized air supply system which contains a measured minimum amount of steam.

In case of the H2P2_5 experiment, the steam concentration was adjusted by injecting steam. After pre-conditioning, a stratified helium layer ($X_{He} \approx 50$ %) was created in the upper vessel region above an elevation of 6000 mm while the pressure was maintained by the venting from the lower section of the PANDA vessel. This procedure allowed to

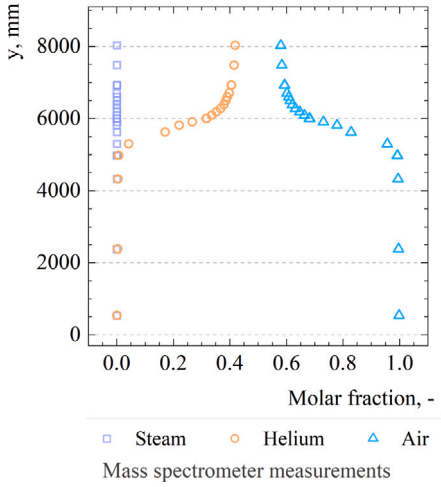

Fig. 3. Initial gas composition at the vessel axis for experiment H2P2_1_2, measured $t = 10$ s before the beginning of the compression.

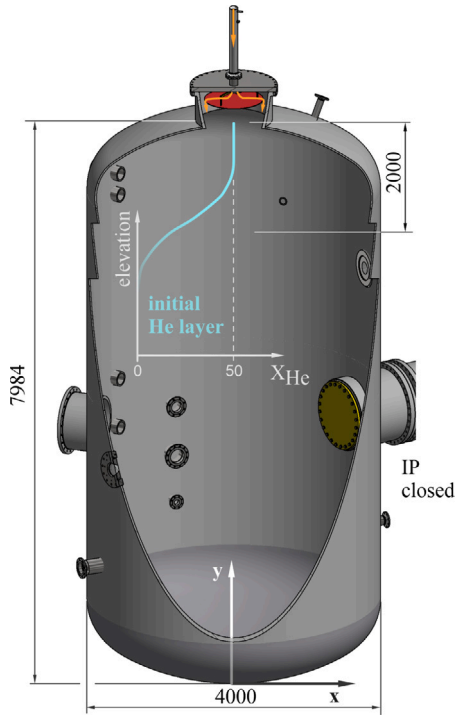

Fig. 4. Illustration of the H2P2 series test configuration, using one isolated PANDA drywell vessel. All dimensions are given in mm.

Table 2
Measurement uncertainties ϵ_e in the H2P2 experiments: temperature T, helium X_{He}, steam concentration $X_{H_2O,l}$ (H2P2_1_2) and $X_{H_2O,h}$ (H2P2_5), pressure p, and the helium mass flow rate $\dot{m}_{He}$.

Quantity	T	p	$X_{H_2O,l}$[a]	$X_{H_2O,h}$[b]	$\dot{m}_{He}$
Units	K	bar	*vol* %	*vol* %	g/s
Typical	383	1	0.1	60	10
Uncertainty ϵ_e	±0.8	±0.01	±0.009	±1	±0.1

[a]The extremely low initial steam concentration was determined using a special humidity sensor and sampling procedure, refer to Kapulla et al. (2022).
[b]In case of the high initial steam concentration, its volume fraction was measured using the mass spectrometer of PANDA. The uncertainty for the helium measurements, X_{He}, is identical to that of $X_{H_2O,h}$.

prevent a temperature and pressure increase within the helium layer formation phase (cf. Fig. 2).

The obtained initial gas mixture, were characterized accurately, to provide initial conditions for code validation purpose. E.g., in Fig. 3, the concentrations measured along the central vessel axis (t = 10 s before the compression phase, see Fig. 2) are visualized for the reference experiment H2P2_1_2. While in the stratified helium layer (y > 6000 mm) the fluid consists of around 40% helium and 60% dry air, below y = 4000 mm there is only dry air ($X_{H_2O} < 0.1$ %).

During the main test sequence, the venting system was closed, and within the compression phase, helium was injected at a mass flow rate of $\dot{m}$ = 10 g/s for a time frame of Δt = 1200 s through a central pipe in the upper man-hole. The hydraulic compression results in a temperature and pressure increase. Subsequent to the helium injection, the so-called decay phase is around Δt = 1800 s. The gas temperature and pressure decrease due to the heat transfer to the vessel structures and were recorded to evaluate the impact of thermal radiation heat transfer (see Fig. 2). The experimental uncertainties associated with measurements of gas and wall temperatures T, helium concentrations X_{He}, vessel pressure p, and helium mass injection rate $\dot{m}_{He}$ were characterized in Paranjape et al. (2018) and are summarized in Table 2.

3. CFD and thermal radiation modeling — theoretical background

For the simulation of the present experiments, the CFD simulation tool *containmentFOAM* is used. It is developed on the background of analyzing transport and mixing phenomena inside and pressurization of large dry PWR containments. It is based on the open source CFD toolbox OpenFOAM, (Kelm et al., 2021). A number of additional, containment specific numerical models and libraries are implemented in *containmentFOAM*. These are (among others): A buoyancy turbulence model, a multi species transport model, a condensation model, a thermal radiation model, and an aerosol transport model. A detailed description of the overarching concepts of *containmentFoam* can be found in Kelm et al. (2021) and a detail description of the thermal radiation heat transfer model is presented in Liu et al. (2022).

The computationally efficient Unsteady Reynolds-Averaged Navier–Stokes (URANS) approach can describe the time averaged turbulence flows in high accuracy, and the turbulence fluctuations are commonly modeled by the standard two equation models (e.g., $k-\omega$ and $k-\epsilon$, Wilcox (2006)). The relevant governing equations for the CFD treatment are the conservation of mass, momentum and total energy. Since the density difference between air and helium is huge in H2P2 experiments, the density of media is calculated by the ideal gas low, not Boussinesq approximation.

$$\frac{\partial \rho}{\partial t} + \nabla \cdot (\rho U) = 0 \tag{1}$$

$$\frac{\partial (\rho Y_i)}{\partial t} + \nabla \cdot (\rho U Y_i) = \nabla \cdot \left[\rho \left(D + \frac{\nu_t}{Sc_t} \right) \nabla Y_i \right] \tag{2}$$

$$\frac{\partial (\rho U)}{\partial t} + \nabla \cdot (\rho U U) = \nabla \cdot \tau - \nabla p + \rho g \tag{3}$$

$$\tau = \rho(\nu + \nu_t) \left[\nabla U + (\nabla U)^T - \frac{2}{3} \delta \nabla \cdot U \right] \tag{4}$$

$$p = \rho R T \tag{5}$$

where ρ is the fluid density; U is the velocity vector; Y_i is the i−th species mass fraction; D is the molecular diffusivity; Sc_t is the turbulent Schmidt number; τ is the Reynolds shear stress; ν is the kinematic viscosity; ν_t is the turbulent kinematic viscosity; δ is the Dirac delta function; g is the free fall acceleration; p is the total pressure; R is the universal gas constant.

The main subject of this paper is the energy equation. In *containmentFoam*, the total enthalpy ($h_{tot} = h + \frac{1}{2}U^2$) used for the energy equation is calculated according:

$$\frac{\partial (\rho h_{tot})}{\partial t} + \nabla \cdot (\rho U h_{tot}) = \rho U \cdot g + \frac{\partial p}{\partial t} + \nabla(\lambda + \lambda_t)\nabla T - \sum_i h_i \nabla \cdot J_i - \nabla \cdot q_r \tag{6}$$

where λ is the thermal conductivity; λ_t is the turbulent thermal conductivity; J_i is the diffusive mass flux of species i; h_i represents the i−th species enthalpy and $-\nabla \cdot q_r$ is the radiative source term.

Neglecting scattering effects, the radiative transfer equation (RTE) within the participating media can be written according (Modest, 2013):

$$\Omega \cdot \nabla I_\eta(r, \Omega) = -\kappa_\eta I_\eta(r, \Omega) + \kappa_\eta I_{b,\eta}(r, \Omega) \tag{7}$$

where Ω [sr] is the solid angle; η [cm^{-1}] is the wave-number; κ_η [m^{-1}] is the absorption coefficient; I_η [$\mathrm{W/(m^2 \cdot sr \cdot cm^{-1})}$] is the spectral intensity; $I_{b,\eta}$ [$\mathrm{W/(m^2 \cdot sr \cdot cm^{-1})}$] is the black body emission spectral intensity. The radiation intensity $I_\eta(r_{wall}, \Omega)$ caused by an opaque wall is given by:

$$I_\eta(r_{wall}, \Omega) = \epsilon I_{b,\eta}(r_{wall}, \Omega) + \frac{1-\epsilon}{\pi} \int_{n \cdot \Omega' < 0} I_\eta(r_{wall}, \Omega') \, |n \cdot \Omega'| \, d\Omega' \tag{8}$$

where ϵ is the surface emissivity and r_{wall} the wall boundary position.

Although thermal radiation heat transfer is not the dominant heat transfer mode, it can significantly affect the temperature distribution and thus change the density field. Therefore, it is necessary to consider radiation heat transfer in containment flows because it can affect the buoyancy driven flows and mixing processes, (Liu et al., 2022). When solving the radiation transfer equation, it is important to consider that (a) the spectral gas properties of infrared active gases (e.g., H_2O and CO_2) strongly depend on the wave-number and (b) the accuracy of thermal radiation modeling. Consequently, modeling of thermal radiation heat transfer in a mixture of transparent and non-transparent gases is a challenging task. Moreover, the absorption coefficient κ_η depends on the partial pressures of the infrared active species (here water vapor) and the temperature of the fluid, (Rivière and Soufiani, 2012). The simplest gray gas model neglects the wavelength dependence and models the absorption coefficient as a constant over the entire infrared spectrum, (e.g., Planck mean absorption coefficient, (Zhang and Modest, 2002)). This gray gas model is an efficient method to estimate thermal radiation source terms in combustion applications. However, the gray gas model is not an accurate model for containment safety analysis because the modeling error introduced by the simplified treatment of the spectral properties can accumulate over the long simulated time frames and affect the prevailing buoyancy-driven transport processes. To also reflect the wavelength dependent variations of the absorption coefficient, the statistical narrow band correlated-k model (SNBCK) was introduced for thermal radiation solvers, which has been shown to be well balanced between efficiency and accuracy, (Rivière and Soufiani, 2012). Rather than resolving the entire wave-number dependence of the absorption coefficient in a small interval with a line-by-line approach (Chu et al., 2012), the SNBCK model reduces the whole spectrum into a finite number of small, discrete wave-number bands with a typical bin size of 50 cm^{-1}. For each band, the non-gray gas property is represented by a set of absorption coefficients $\kappa_j^{\eta_0}$ and Gaussian weights ω_j. Thus, for a (locally) homogeneous media at a given temperature, pressure and gas composition, the transmissivity is given by the integral of the absorption coefficient κ_η times the path length L over the wave-numbers. To finally calculate the total transmissivity $\tau_{\Delta\eta}$, the correlated-k method employs the re-ordering method to convert the wave-number integration into the absorption-coefficient-integration (Rivière and Soufiani, 2012):

$$\tau_{\Delta\eta} = \frac{1}{\Delta\eta}\int_{\eta_0}^{\eta_0+\Delta\eta} e^{-\kappa_\eta L} d\eta \approx \sum_{j=1}^{N_G} w_j e^{-\kappa_j^{\eta_0} L} \tag{9}$$

where $\tau_{\Delta\eta}$ is the mean transmissivity; η_0 is the band wave number; $\Delta\eta$ is width of the spectral bands; L is the path length; N_G is the quadrature number; $\kappa_j^{\eta_0}$ and ω_j are the absorption coefficient and the quadrature weight. It is noted, that 7 Gauss quadrature points are sufficient to give a good approximation. For the implementation in *containmentFOAM* a new steam SNBCK database was generated using the HITRAN2016 database, (Liu et al., 2022).

After condensing the non-gray gas properties to a computationally manageable scale, the second challenge is to implement a reliable and efficient radiation solver which can cope with gas flows in complex geometries. Generally speaking, the P1 method, simplifies the radiative transfer equation into a diffusion equation for optically thick media and was applied in several thermal radiation analyses over the last decade (Modest, 2013). However, the P1 method can significantly over-estimate the strength of thermal radiation using this diffusion simplification. To increase the numerical accuracy and stability, a Monte Carlo method for solving radiative heat transfer using the new SNBCK model was implemented for the present investigations. The Monte Carlo method solves the integral form of radiative transfer equation, Modest (2013). Therefore, all kinds of physical scenarios e.g., soot/aerosol scattering, spectral gas property and non-gray-wall emissivity, can be considered in the Monte Carlo method without significantly increasing the computational time Modest (2013).

For the implementation of the Monte Carlo method, the net radiation source term is determined through the balance between absorbed and emitted energy. While the emission is related only to the fluid temperature and the spectral gas property, the absorption energy for an element within the computational domain is a complex function of the absorption coefficient, the temperature distributions and boundary conditions. Thus, the Monte Carlo method requires to calculate the view factor matrix $\mathcal{F}$ for each control volume and boundary surface. To meet this requirement, the radiative source term at cell i can be described according (Tessé et al., 2004) with:

$$-\nabla \cdot q_r^{cell\,i} = \frac{abs. - emis.}{V_i} = \frac{1}{V_i}\left[\sum_{k=1}^{N_{cell}+N_{face}} Q_k \mathcal{F}_{k\to i} - Q_i\right] \tag{10}$$

For the radiative wall heat flux at a surface j it follows:

$$q_r^{surf.\,j} = \frac{abs. - emis.}{S_j} = \frac{1}{S_j}\left[\sum_{k=1}^{N_{cell}+N_{face}} Q_k \mathcal{F}_{k\to j} - Q_j\right] \tag{11}$$

where V_i is the volume of cell i; Q_i is the radiation emission from cell i; S_j is the area of surface j; Q_j is the radiation emission from surface j; $\mathcal{F}_{k\to i}$ and $\mathcal{F}_{k\to j}$ are the view factors. The view factor matrix $\mathcal{F}_{k\to i}$ describes the fraction of emitted energy from a surface or cell k that reaches the element i including the non-gray gas attenuation and boundary surface absorption. It is worth noting, that the view factor $\mathcal{F}_{k\to i}$ is a function of the media non-gray property, surface emissivity and geometry. The total radiation emission from cells and boundary surfaces can be determined if the total pressure, temperature and molar fractions are given by the CFD solver, Tessé et al. (2004). But, the net energy absorbed within cell i is difficult to quantify due to the complex interactions of thermal radiation and transport processes of the non-gray gas medium. It is important to note that, different from convective or diffusive transport, radiation can transfer energy over long distances within an optically thin media. The view factor matrix $\mathcal{F}$ is determined by the Monte Carlo method by tracking a large amount of photons within the computational domain Tessé et al. (2004). The only limitation of the Monte Carlo method is the statistical error. It is proportional to one over the square root of the number of photons and thus can only be reduced by drastically increasing the number of photons which comes along with a corresponding increase in computational effort. To overcome this drawback to some extent, a couple of optimization methods and efficient algorithms have been integrated in the radiation model library of *containmentFOAM* Liu et al. (2022).

3.1. Modeling strategy

The simulations were performed with a full 3D mesh of the vessel of the PANDA facility, Fig. 5. The mesh resolution for the 3D model is evenly distributed in the bulk and refined towards the vessel walls. The helium is injected through a central feed line and impinges on a baffle plate to disperse the momentum to some extent. In preliminary simulation runs with a simplified injection, we placed the helium inlet in the annular gap between plate and vessel wall. However, this simplification neglects the dispersed momentum, which results in an increased heat transfer between the hot vessel walls and the injected colder helium. Therefore, the impinging flow must be resolved and the injection region including the circular disk is resolved by the mesh. The mesh quality has been optimized in terms of face angle, aspect ratio and volume ratio and is well above the minimum quality recommendations in the best practice guidelines, (NEA, 2012b). The mesh independence of the resulting gas temperature field was assessed with a systematically refined (double resolution, eight times more cells) reference mesh. The mesh has more than 2.6 million cells or nodes which is enough to resolve the gas compression process. Furthermore, the H2P2 experiment series are characterized by low fluid velocities to isolate the thermal radiation effects with best efforts. The main focus

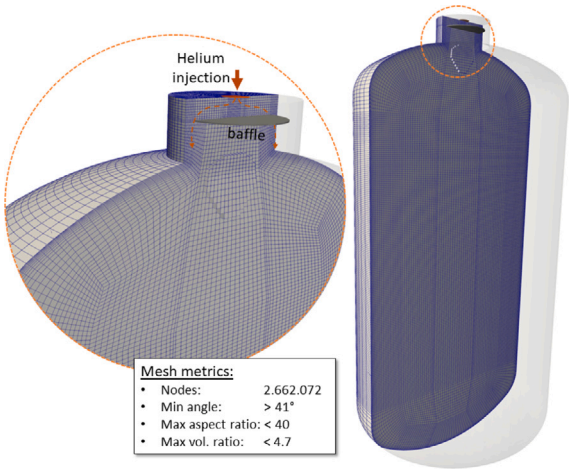

Fig. 5. 3D grid used for the simulation of the H2P2 experiments together with main characteristics.

of this paper is to evaluate the impact of different thermal radiation models for containment atmosphere simulations.

In both experiments H2P2_1_2 and H2P2_5, the helium is injected at room temperature (293 K) with a constant mass flow rate (10 g/s) via the vertical centered tube at the top of the vessel, Fig. 4. For experiment H2P2_1_2, the initial fluid and wall temperatures are at room temperature T_r; while the initial temperature level for H2P2_5 is at an elevated temperature T_{el}. In both cases, no bulk or wall condensation occurs. Consequently, the wall temperature is assumed to remain constant at its initial value during the transient compression. The initial helium and H_2O distributions inside the vessel are specified for the simulations according to the measured vertical profile, obtained by circumferential averaging of the available sensors, see Fig. 3. The injection boundary condition is modeled by prescribing the recorded history of the helium mass flow rate and its temperature. The turbulent kinetic energy and eddy frequency are calculated assuming a turbulent intensity of $u'/U = 5\%$ and an eddy viscosity ratio of 10. The walls are treated as hydraulically smooth using a no-slip boundary condition. Their emissivity ϵ is set to 0.3 based on the measurement of a dry steel sample at PSI.

The physical models are defined according to the baseline model implemented in *containmentFOAM* which is described in Kelm et al. (2021). The URANS approach is adopted and closed with the k-ω SST model including source terms to account for production and dissipation of turbulence due to buoyancy forces. The fluid is considered as an ideal gas with temperature dependent transport properties. The pressure and species are determined within the PIMPLE loop and the thermal library updates the density field according to the ideal gas equation. Non-gray gas radiation is modeled using the Monte Carlo solver mentioned above together with the SNBCK model for the fluid mixture spectral absorption characteristics, see for a more in depth discussion (Liu et al., 2022). Between 20 and 40 photon trajectories are followed per cell (about 100'000'000 trajectories in total) to calculate and update the radiation source terms every 5 s of physical time.

The interdependence between the hydraulic and the thermal radiation field was investigated for example in combustion modeling with a much higher dynamic and a stronger coupling of both fields compared with the conditions in a containment with much lower flow velocities. For the combustion modeling is was concluded that updating the thermal radiation solver every 100 fluid time steps is sufficient, see Zhang et al. (2022). Own preliminary tests for the conditions under investigation have demonstrated that it is even possible to relax the update speed to every 500 fluid time steps; no significant difference between 100 versus every 500 CFD time step was monitored.

The numerical methods used have 2nd order accuracy, as described in Kelm et al. (2021). The validation cases are calculated with a time step of $\Delta t = 0.005$ s, which corresponds to a Courant number (CFL) of less than one. The convergence criteria for the linear solvers was set to 10^{-6}, while the initial residuals had to be below 10^{-4} for the PIMPLE iterations. A couple of simulation runs were conducted for the purpose of model assessment and validation.

In the following, we present 3D simulation runs to illustrate the impact of certain modeling choices. The effects of gas radiation is highlighted using two simulations (H2P2_1_2 and H2P2_5) where the radiative transport is completely neglected; these are the 'nr' or 'norad' cases. The simulation using the finite volume Monte Carlo approach together with the SNBCK non-gray gas model is labeled as 'r' or 'SNBCK'. The gray absorption coefficient is calculated from the weighted-sum-of-gray-gases model (Smith et al., 1982). The steam absorption coefficient for the gray gas model is 5 m^{-1}. For comparison purposes we additionally provide results for the widespread used P1 radiation model (Modest, 2013).

In addition, for the reference experiment (H2P2_1_2), we present an adiabatic calculation which sheds some light on the initial phase of the compression; this is labeled as 'ad'. In the experiments considered, the convective flows are weak and the molecular diffusion D_m is of the same or higher order of magnitude than the turbulent diffusion D_t. Therefore, it was necessary to eliminate the molecular diffusion to compensate the artificial numerical diffusion for the H2P2 test cases. A series of simulations were performed using different numerical setting for the CFD and Monte Carlo solvers to assess and ensure the independence of the results from chosen numerical parameters such as the number of photon trajectories, the update frequency of the radiation source term, spatial and temporal discretization schemes, and numerical solution approaches.

4. Results and discussion

In this section, selected experimental and simulation results of the gas temperature obtained during both compression and decay phases of the experiments H2P2_1_2 and H2P2_5 are presented, compared and discussed, see Table 1.

Temperature maps created from all temperature measurements in the x–y plane (cf. Fig. 4) are shown for the end of the compression phase ($t = 1200$ s) and for the reference case H2P2_1_2, which started at room temperature T_r and had the lowest steam content, Fig. 6. Provided are numerical results for the SBNCK and the P1 model as well as the result without any radiation (norad).

The temperatures were normalized with the temperature T_0 at the beginning of the compression. Thus, we present the maximum excess temperature caused by the compression due to the injection of helium from the top.

Both, experimental and numerical results have in common, that the temperature in the top part of the vessel ($y \gtrsim 5000$ mm) is almost homogeneous and only slightly increased compared to the initial temperature. This homogenization is caused by the momentum of the helium influx with the initial helium layer, which could not be completely dispersed by the baffle plate, see Fig. 4 and for more details (Kapulla et al., 2022). This mechanism counteracts the expected temperature increase from the compression in the vessel dome. At the transition location separating the temperature field between the upper and the lower part of the vessel ($y \approx 5000$ mm), we find a strong temperature gradient and a significantly higher temperature below $y = 5000$ mm.

This zone with higher temperatures extends down to about $y \approx 3000$ mm, and in the lower part of the vessel we find only moderately elevated temperatures, which are hardly affected by the compression. The zone with elevated temperatures is characterized by a strong layering of the temperature distribution — except for the temperatures

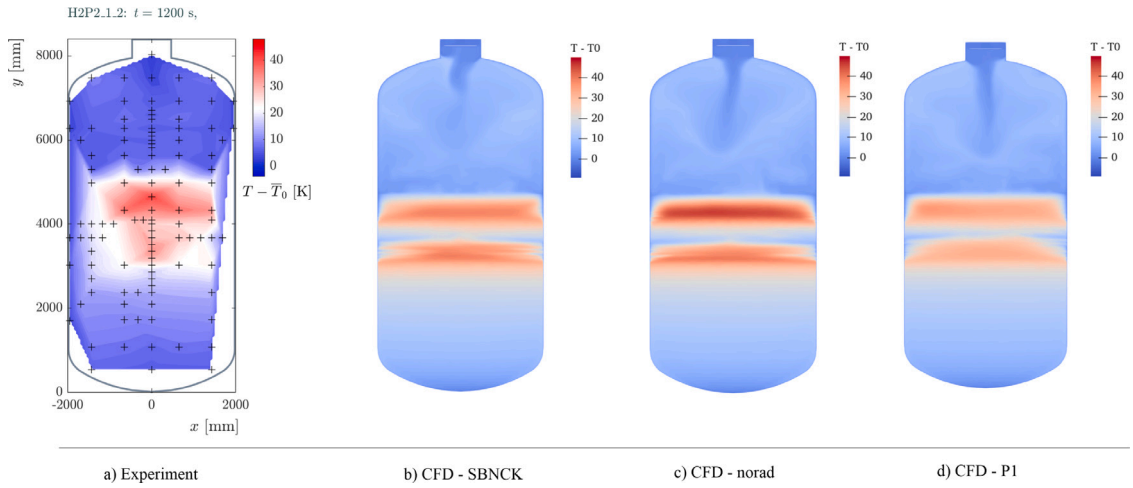

Fig. 6. Comparison of the experimental, (a), and numerical, (b) to (d), temperature maps at the end of the compression phase at $t = 1200$ s recorded in the x–y plane for the reference case H2P2_1_2. For the experiment, thermocouple locations are indicated by +. Temperatures are normalized with the initial temperature T_0. For the CFD results we compare the cases using the radiation model SBNCK (b), using no radiation model at all (c) and the model P1 (d).

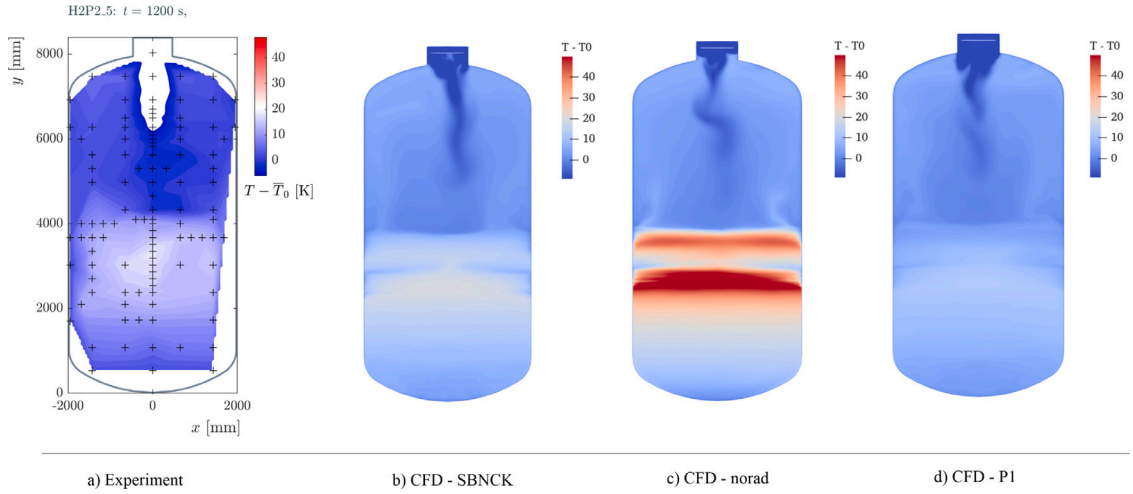

Fig. 7. Comparison of the experimental, (a), and numerical, (b) to (d), temperature maps at the end of the compression phase at $t = 1200$ s recorded in the x–y plane for the case H2P2_5. For the experiment, thermocouple locations are indicated by +. Temperatures are normalized with the initial temperature T_0. For the CFD results we compare the cases using the radiation model SBNCK (b), using no radiation model at all (c) and the model P1 (d).

close to the vessel walls, because due to its high thermal inertia the vessel remains colder throughout the transient.

Comparing the temperature fields obtained for different modeling strategies (SBNCK, P1 and norad), we note that both SBNCK and P1 result in slightly lower temperatures at the end of the compression phase compared with the norad case, Fig. 6 . This is an indication, that even the very low steam content of 0.1% for the reference experiment H2P2_1_2 (which is considered having a dry atmosphere), finally has some impact onto the resultant temperature maps, compare Figs. 6(b) and (d) with (c). Finally, we find that the P1 model – which is diffusion based – results in a more homogeneous temperature map with a less pronounced temperature differentiation in the high temperature regions.

The main differences between the experiment and the numerical calculation are (i) the slightly lower location of the sharp temperature gradient between the upper and lower part of the vessel (see also Fig. 12 and the corresponding discussion), (ii) the slightly higher excess temperature and iii) the higher temperature in the lower part of the vessel obtained in the CFD calculation. The corresponding temperature distributions extracted in the vessel axis ($x = 0$ mm) can be seen in Fig. 8(a). In summary, we can conclude, that neglecting radiation effects is a valid modeling strategy when there are only marginal concentrations of radiation active gases such as steam — as for the reference experiment H2P2_1_2.

The corresponding temperature maps at the end of the compression phase can be found for the H2P2_5 case in Fig. 7 — again the experiment is compared with the modeling strategies SBNCK, P1 and norad. H2P2_5 started at elevated temperatures and with a significantly higher initial steam content, Table 1. Expecting radiation effects to play a dominant role, the main CFD calculation was performed using the SNBCK model, as described in Section 3. To highlight the importance of radiation to the corresponding numerical simulation, we compare numerical results in which radiation modeling was turned off (Fig. 7 c).

In contrast to the reference experiment, the location of the gradient region separating the upper and lower part of the vessel ($y \approx 4000$ mm) is well predicted, while the temperature rise of the CFD calculation is again slightly higher compared with the experiment, Figs. 7(a) versus (b). Finally, neglecting the radiative modeling leads to a much higher excess temperature, which differs by almost 20 K from the result obtained with the SNBCK model, Figs. 7(b) versus (c). The P1 model significantly over-estimates the effect of radiation heat transfer resulting in a temperature field with lower temperatures compared with the SBNCK model, compare Figs. 7(b) versus (d). These results demonstrate the importance of radiation modeling in the presence of absorbing (and

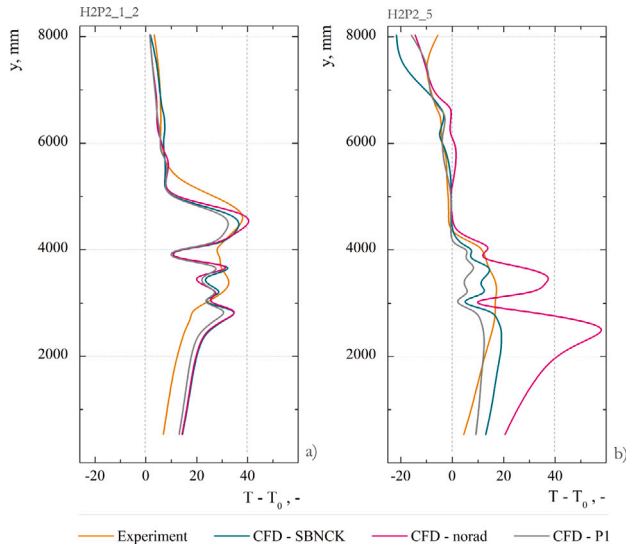

Fig. 8. Comparison of the excess temperature profiles $T_e = T - T_0$ extracted in the vessel axis for H2P2_1_2 (a) and H2P2_5 (b) at the end of the compression phase $t = 1200$ s. Data taken from Figs. 6 and 7.

emitting) media for the accuracy of the numerical results. For H2P2_5 conducted at increased temperature level, it is relevant to note that the temperature of the injected helium used for compression was less than that used to form the initial helium layer. Therefore, the flow pattern downstream the baffle plate is locally enhanced by negative buoyancy forces, resulting in a remarkable downwards momentum of the injected helium mass, as seen by the white cropped range (experiment) and the lower temperature (CFD) seen at the upper region of the facility near the man-hole (see Fig. 7).

To complement the discussion based on the temperature fields evaluated at the end of the helium injection/compression phase ($t = 1200$ s), the excess temperature profiles $T_e = T - T_0$ extracted in the vessel axis for H2P2_1_2 and H2P2_5 are presented in Fig. 8. For the CFD calculation, the temperatures were taken from locations where also thermocouples were installed. These locations are marked with + in Figs. 6 and 7. For experiment H2P2_1_2, we find a very good agreement between the experimental and numerical results from the top of the vessel up to a height of about 4000 mm, Fig. 8(a). Below this height, the numerical results show (i) a slightly stronger modulation of the temperature and (ii) a slightly weaker temperature drop towards the bottom of the vessel. For the H2P2_5 case in Fig. 8(b), the numerical results agree even better with the experiments — with the exception of the region at the bottom of the vessel below 2000 mm. The importance of taking radiation phenomena into account is shown by the much higher temperatures obtained for the 'norad'-case. The peak temperature is higher by more than a factor of two compared to both the experimental results and the simulation using the SBNCK model. The temperature difference between the P1 and the SNBCK model is considerable large for the H2P2_5 (see Fig. 8(b). Thus, it is concluded that a suitable non-gray gas model is vital for thermal radiation analyses in containment flows.

To emphasize the transient nature of the compression and decay phase, selected temperature time traces extracted at four locations in the upper half of the vessel axis are compared in Fig. 9 for (H2P2_1_2 a) and (H2P2_5 b). For the reference experiment (H2P2_1_2), the calculation includes the no radiation (nr) and the adiabatic (ad) cases, and for H2P2_5 the radiation using the SNBCK model (r) and the 'norad' (nr) cases. For the H2P2_1_2 we observe for the numerical calculations consistently and for the experiment below the helium stratification initially ($t < 200$ s) a temperature increase that is almost identical to that of the adiabatic calculation, Figs. 9(γ) and (δ). This is, during the time, where the temperature increase due to compression is sufficiently small and the heat transfer to the vessel walls can be neglected. Past ($t \gtrsim 300$ s - CFD) and ($t \gtrsim 200$ s - experiment), the temperature evolution deviates significantly from an adiabatic compression, resulting in much lower temperatures. On a much shorter time scale, similar conclusions can be drawn from the respective temperature traces for H2P2_5, Fig. 9(b). In this experiment with the much higher humidity, the initial time where the compression can be treated as adiabatic ($0 < t \lesssim 100$ s) is considerably shorter, since radiative effects play a dominant role for heat transport already in the early phase of the experiment. Below $y \lesssim 5000$ mm we again find considerable higher temperatures for the norad compared with the radiation temperature traces. In addition, we find on average for H2P2_5 a much better agreement between the experimental and the numerical (CFD, r-SNBCK) results compared with H2P2_1_2 (CFD, nr), Figs. 9(α) to (δ).

To make the differences even clearer, we show a comparison of the experimental and numerical excess temperature $T_e = T - T_0$ from the vessel axis in the form of a heat-map covering the compression and decay phase for case H2P2_1_2 (a) and H2P2_5 (b) as a function of time, Fig. 10. For the CFD results we used exactly those locations where thermocouples were available for the experiments. For the CFD results, we plot the 3D 'norad' (H2P2_1_2) and the 3D 'SBNCK' (H2P2_5) case. To illustrate the dissimilarity, we also give the difference of T_e between the experimental and numerical results ($Exp - CFD$). The downward movement of the stratification interface between the helium layer and the compression zone below it is shown as a white line.

Overall, we find the temperatures for the experiments are more homogeneous compared to the numerical results — for both cases (H2P2_1_2 and H2P2_5). For example, the CFD calculations exhibit a significant and persisting lower excess temperature around $y \approx 4000$ mm, which does not seem to be affected by either the compression or the decay phase — while the helium stratification experiences a considerable downwards movement through the injection of the helium from above. Looking at the differences in the observed excess temperatures, it is precisely at these points in the 'layering' where the largest discrepancies are located. Even though this is also true to some extent for the boundary zone between the helium stratification and the underlying compression zone, we can conclude that the compression and decay phases are well captured for both cases, Figs. 10(a-iii) and (b-iii).

The downwards movements of the helium rich layer above the compression zone are compared for experiments H2P2_1_2 and H2P2_5 in Fig. 12. Their locations were determined using image processing techniques that identify the steepest gradient from the corresponding data in Fig. 10. The error bars indicate the uncertainty of the chosen method. For experiment H2P2_1_2, the helium stratification is located at $y \approx 5000$ mm at the end of the compression, while for H2P2_5 it is at $y \approx 4400$ mm. Overall, we find a reasonable agreement between the experiments and the numerical calculations for both cases considered.

To obtain an integral temperature metric characterizing the transient evolution of both compression phase and decay phase by means of a single scalar, a weighted temperature T_w is calculated using the sensors on the vessel rotation axis $T(t, y, x = 0)$ within the elevation range of $y \in [531, 4100]$ in the integral:

$$T_w(t) = \frac{1}{\Delta y} \int_{y=531}^{y=4100} \left\{ T(t,y) - \overline{T}_0(t=0) \right\} dy \,, \tag{12}$$

which can be transformed to the discrete form:

$$T_w(t) = \frac{1}{\Delta y} \sum_{i=1}^{n} \left\{ T_i(t,y) - \overline{T}_0(t=0) \right\} \left(y_{i+1} - y_i \right) \,. \tag{13}$$

The corresponding results are normalized with the height of the integration window ($\Delta y = 3569$ mm). The index $n = 18$ determines to the position of the thermocouple at $y = 4100$ mm in the axis of the vessel. The upper bound was chosen to be the elevation where the

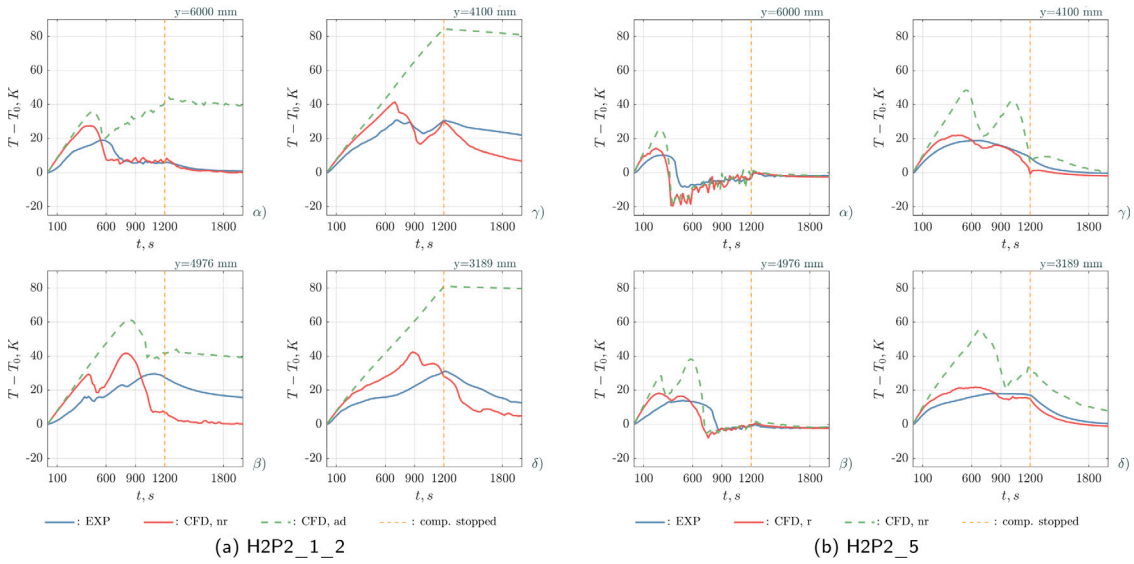

Fig. 9. Selected temperature time traces extracted at four locations in the upper half of the vessel axis for case H2P2_1_2 (a) and H2P2_5 (b). Compared are the experimental and the calculated results. For the reference experiment (H2P2_1_2) the calculation comprises the 'norad–nr' and the adiabatic (ad) cases and for H2P2_5 the radiation (r) and the 'norad' (nr) cases. All normalized temperature signals cover the initial compression and the following decay phase past $t = 1200$ s.

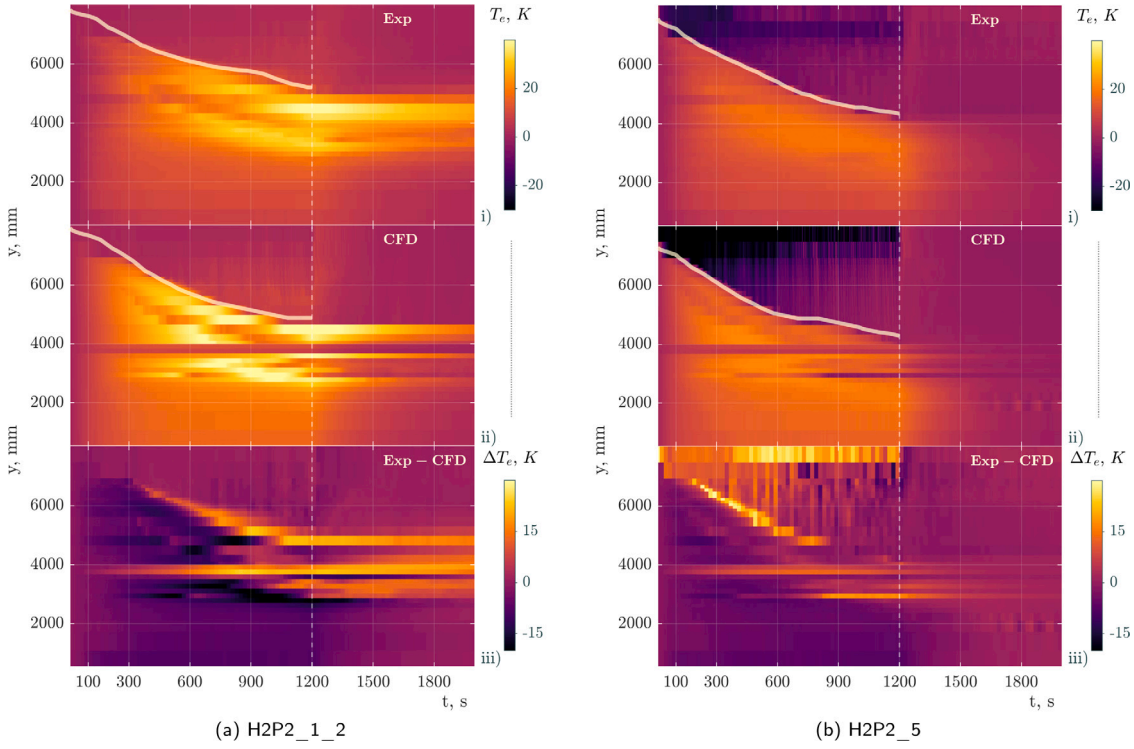

Fig. 10. Comparison of the experimental and numerical excess temperature $T_e = T - T_0$ taken from the vessel axis presented as a heat-map covering the compression and decay phase for case H2P2_1_2 (a) and H2P2_5 (b). For the CFD results we present the 3D 'norad' (H2P2_1_2) and the 'SBNCK' (H2P2_5) cases. The experimental (i) and numerical (ii) results share the same color bar. To indicate the differences, we additionally provide the difference of T_e between the experimental and numerical results ($Exp - CFD$). The downward movement of the helium stratification front and the compression zone (continuous line) as well as the end of the compression phase (vertical dashed line) is indicated.

injected helium into the stratified helium layer has no effect onto the calculation of T_w on average and for the two experiments, see also the location of the helium stratification at the end of the compression phase in Fig. 12. This is particularly important for experiment H2P2_5, where the injected helium had a lower temperature compared with the helium stratification. See for comparison Fig. 7(b) and for more details (Kapulla et al., 2022). The corresponding experimental and numerical results for T_w are shown in Fig. 11. Two regions with distinct temperature rise characteristics can be identified for both experiments. A first phase (E) up to approximately $t \approx 300$ s with a steep temperature rise and a second phase for the rest of the compression phase with either a moderate temperature rise (H2P2_1_2) or even with an evolution towards an asymptotic value (H2P2_5). Moreover, these results show that the integral temperatures T_w for the CFD calculations during the compression phase are consistently higher than the experimental results for both test cases. This difference is much smaller for H2P2_5. In

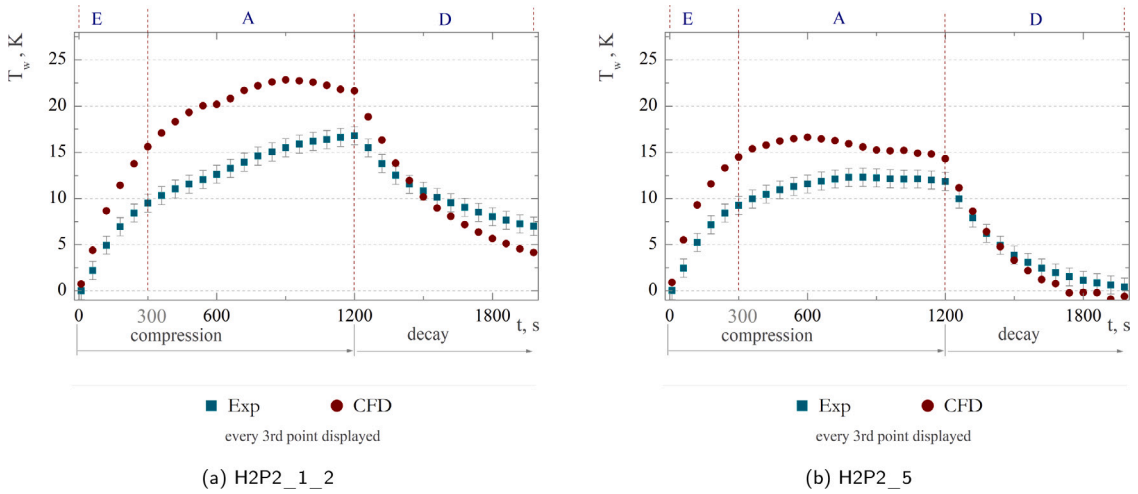

Fig. 11. Comparison of the experimental (a) and numerical (b) temperature T_w, averaged vertically according Eq. (13) for both compression and decay phases for H2P2_1_2 (a) and H2P2_5 (b).

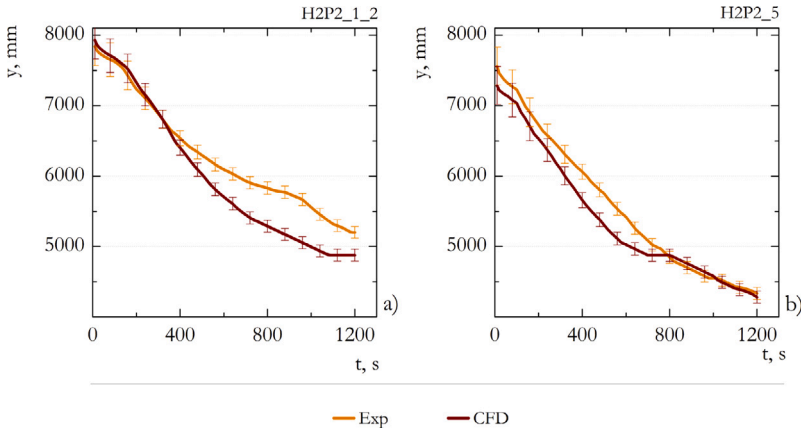

Fig. 12. Comparison of the experimentally and numerically determined He layer downwards movement during the compression phase for case H2P2_1_2 (a) and H2P2_5 (b). Data are taken from Fig. 10.

the decay phase, we find a better agreement for H2P2_5 compared to H2P2_1_2.

To provide an explanation for the discrepancies between the experimental and CFD results using T_w as a metric, we would like to recall the purpose of this integral temperature approach:

- Goal was, to reduce and condense the complexity of the heat-maps of Fig. 10 into a single number, capable to represent the transient differences between experimental and CFD results.
- What the metric T_w essentially does, is to provide a spatially normalized temperature representing the heat-up in the lower part of the vessel — extending down to the vessel bottom!
- Since the upper integration bound with $y = 4100$ mm was chosen very conservative, we miss – in parts – the good match between experiments and CFD results at intermediate elevations of the vessel, while we emphasize especially for H2P2_1_2, the higher CFD temperature results below $y < 3000$ mm as depicted in Fig. 8 at the end of the compression phase.
- Finally, the reason why the CFD results over predict the temperature increase at the bottom of the vessel during the compression phase, is subject of ongoing discussions and refinements.

To conclude the discussion, it should be noted that all numerical results presented are from 3D calculations, see Fig. 5. The original experimental setup with co-axial injection of the helium from the top placed some emphasis on the 2D treatment of the various experiments, which significantly reduces computational costs, for details on the experiments see Kapulla et al. (2022). To proof this concept, we compare the temperatures in the vessel axis at the end of the compression phase based on 2D versus 3D calculations in Fig. 13. With the exception of the calculation of the temperatures in the upper part of the vessel for the H2P2_5 experiment, we find a very good agreement, justifying a 2D treatment of the other cases in the experimental series H2P2.

5. Conclusions and outlook

Previous validation work indicated the significance of radiative heat transfer. Unfortunately, these experiments included multiple interacting physical phenomena such as condensation, convection, radiation and turbulence which made it difficult to isolate, test and evaluate different radiation modeling strategies.

To address this gap, two H2P2 series experiments – H2P2_1_2 (no steam) and H2P2_5 (60% steam) – are discussed to evaluate and validate a Monte Carlo method with the SNBCK, non-gray gas model implemented in *containmentFoam* in the present work. This approach constitutes a feasible and efficient radiation modeling strategy for containment flows. The analysis generally confirms the validity of the radiation modeling approach and consistent representation of the phenomena related to the expansion of the helium layer and the increase in gas temperature during the compression phase. Remaining differences are related to the gas temperature in the helium layer resulting from the

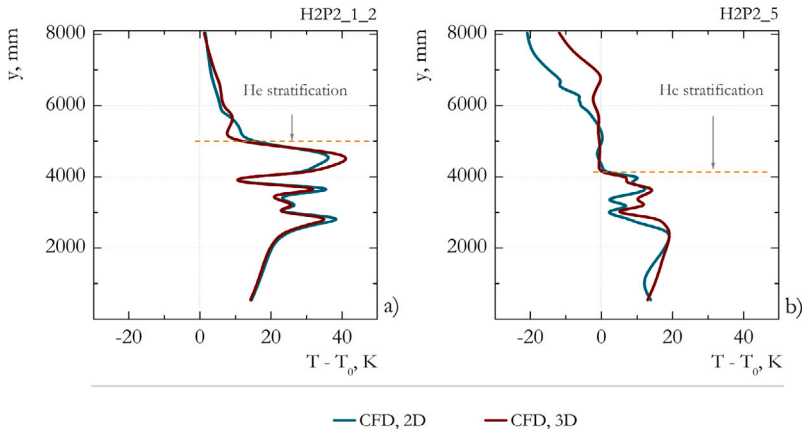

Fig. 13. Comparison of the CFD modeling in 2D versus 3D in terms of the excess temperature $T_e = T - T_0$ in the vessel axis at the end of the compression phases (t = 1200 s). The location of the stratification interface between the helium layer and the compression zone below is indicated.

injection of cold helium into a hot environment and the strong effect of numerical diffusion in the helium–air interaction region. The results suggest a detailed evaluation of the CFD numerical uncertainty for the simulation of the H2P2 series. Ongoing work also includes analysis to clarify the effect of pressure, temperature and helium concentration in the gas mixture during the injection procedure. However, it is confirmed that when thermal radiation is neglected in the H2P2_5 case, the temperature rise is significantly over-predicted by a factor of two compared to the application of the SNBCK model. The unreasonable P1 gray gas model may result in a too homogeneous temperature field in simulations. Therefore, it is recommended to apply a more accurate thermal radiation solver in containment flows as the suggested SBNCK model. Moreover, the computational effort considering CFD and non-gray gas radiation is feasible with the tailored Monte Carlo and SNBCK model, which serves as a basis for future assessment of simpler and more efficient radiation modeling strategies.

CRediT authorship contribution statement

Ralf Kapulla: Conceptualization, Formal analysis, Investigation, Data curation, Writing – original draft, Visualization, Supervision. **Liu Xiongguo:** Conceptualization, Investigation, Data curation, Software, Writing – original draft, Methodology. **Stephan Kelm:** Conceptualization, Writing – review & editing, Software, Investigation, Project administration. **Ulrich Doll:** Validation, Formal analysis, Writing – review & editing. **Sidhart Paranjape:** Investigation, Formal analysis, Data curation, Visualization. **Domenico Paladino:** Funding acquisition.

Declaration of competing interest

The authors declare that they have no known competing financial interests or personal relationships that could have appeared to influence the work reported in this paper.

Data availability

Data will be made available on request.

Acknowledgments

The authors would like to thank Max Fehlmann (25. May 1960; † 30.11.2021) and Simon Suter for their engaged support in conducting these experiments — even during rather challenging COVID 'lockdown' periods. Without their profound knowledge of the PANDA facility and their creativity in finding a feasible technical solution for each scientific problem, it would not have been possible to obtain the results documented in this article. The authors also would like to thank the members of the Management Board and the Program Review Group of the OECD/NEA HYMERES-2 project for their continued confidence in the perspectives the PANDA experiments can provide; and their help to evaluate the results.

References

Ahmed, U., Chakraborty, N., Klein, M., 2021. Int. J. Heat Fluid Flow 92, 108881. http://dx.doi.org/10.1016/j.ijheatfluidflow.2021.108881.

Amend, K., Klein, M., 2020. Nucl. Eng. Des. 366, 110745. http://dx.doi.org/10.1016/j.nucengdes.2020.110745.

Andreani, M., Badillo, A., Kapulla, R., 2016. Nucl. Eng. Des. 299, 59–80. http://dx.doi.org/10.1016/j.nucengdes.2015.12.029, CFD4NRS-5.

Andreani, M., Gaikwad, A.J., Ganju, S., Gera, B., Grigoryev, S., Herranz, L.E., Huhtanen, R., Kale, V., Kanaev, A., Kapulla, R., Kelm, S., Kim, J., Nishimura, T., Paladino, D., Paranjape, S., Schramm, B., Sharabi, M., Shen, F., Wei, B., Yan, D., Zhang, R., 2019. Nucl. Eng. Des. 354, 110177. http://dx.doi.org/10.1016/j.nucengdes.2019.110177.

Andreani, M., Kapulla, R., Kelm, S., Paladino, D., Paranjape, S., 2020. J. Nucl. Eng. Radiat. Sci. 6 (2), http://dx.doi.org/10.1115/1.4046296, 021110.

Andreani, M., Kapulla, R., Zboray, R., 2012. Nucl. Eng. Des. 249, 71–81. http://dx.doi.org/10.1016/j.nucengdes.2011.06.004.

Bestion, D., 2017. A state-of-the-art report on scaling in system thermal-hydraulics applications to nuclear reactor safety and design. (Technical Report R(2016)14), NEA/CSNI.

Cesari, S., Emmi, G., Bottarelli, M., 2022. Appl. Therm. Eng. 206, 118119. http://dx.doi.org/10.1016/j.applthermaleng.2022.118119.

Chu, H., Liu, F., Zhou, H.-C., 2012. Int. J. Therm. Sci. 59, 66–74.

Cilliers, A., 2013. Ann. Nucl. Energy 62, 326–332. http://dx.doi.org/10.1016/j.anucene.2013.06.037.

Dabbene, F., Brinster, J., Abdo, D., Porcheron, E., Lemaitre, P., Mignot, G., Kapulla, R., Paranjape, S., Kamnev, M., Khizbullin, A., 2015. ICAPP 2015 - International-Congress on Advances in Nuclear Power Plants, May 2015, Nice, France. pp. paper 15148, cea–02509081.

Dehbi, A., Kelm, S., Kalilainen, J., Mueller, H., 2019. Nucle. Eng. Des. 341, 176–185. http://dx.doi.org/10.1016/j.nucengdes.2018.10.025.

ERCOSAM, 2014. Containment thermal-hydraulics of current and future LWRs for severe accident management. Funded under: FP7-EURATOM-FISSION, Grant agreement ID: 249691.

Filippov, A.S., Grigoryev, S.Y., Tarasov, O., 2016. Nucl. Eng. Des. 310, 175–186. http://dx.doi.org/10.1016/j.nucengdes.2016.10.003.

Fujisawa, N., Liu, S., Yamagata, T., 2021. Eng. Failure 124, 105388. http://dx.doi.org/10.1016/j.engfailanal.2021.105388.

Gordon, I., Rothman, L., Hill, C., Kochanov, R., Tan, Y., Bernath, P., Birk, M., Boudon, V., Campargue, A., Chance, K., Drouin, B., Flaud, J.-M., Gamache, R., Hodges, J., Jacquemart, D., Perevalov, V., Perrin, A., Shine, K., Smith, M.-A., Tennyson, J., Toon, G., Tran, H., Tyuterev, V., Barbe, A., Császár, A., Devi, V., Furtenbacher, T., Harrison, J., Hartmann, J.-M., Jolly, A., Johnson, T., Karman, T., Kleiner, I., Kyuberis, A., Loos, J., Lyulin, O., Massie, S., Mikhailenko, S., Moazzen-Ahmadi, N., Müller, H., Naumenko, O., Nikitin, A., Polyansky, O., Rey, M., Rotger, M., Sharpe, S., Sung, K., Starikova, E., Tashkun, S., Auwera, J.V., Wagner, G., Wilzewski, J., Wcislo, P., Yu, S., Zak, E., 2017. J. Quant. Spectrosc. Radiat. Transfer 203, 3–69. http://dx.doi.org/10.1016/j.jqsrt.2017.06.038, HITRAN2016 Special Issue.

Kapulla, R., Paranjape, S., Doll, U., Kirkby, E., Paladino, D., 2022. Nucl. Eng. Technol. http://dx.doi.org/10.1016/j.net.2022.07.001.

Kapulla, R., Paranjape, S., Fehlmann, M., Suter, S., Doll, U., Paladino, D., 2021. Nucl. Eng. Technol. http://dx.doi.org/10.1016/j.net.2021.12.032.

Kelm, S., Kampili, M., Liu, X., George, A., Schumacher, D., Druska, C., Struth, S., Kuhr, A., Ramacher, L., Allelein, H.-J., et al., 2021. Fluids 6 (3).

Kelm, S., Müller, H., Allelein, H.-J., 2016. Proc. CFD4NRS-6, , Boston, Massachusetts, USA, September 13-15, 2016.

Li, Y., Zhang, H., Xiao, J., Travis, J., Jordan, T., 2018. Ann. Nucl. Energy 114, 1–10. http://dx.doi.org/10.1016/j.anucene.2017.11.047.

Liu, X., Kelm, S., Kampili, M., Kumar, G.V., Allelein, H.-J., 2022. Nucl. Eng. Des. 390, 111689. http://dx.doi.org/10.1016/j.nucengdes.2022.111689.

Liu, F., Sun, Z., Ding, M., Bian, H., 2021. Int. J. Hydrogen Energy 46 (73), 36477–36502. http://dx.doi.org/10.1016/j.ijhydene.2021.08.151.

Modest, M.F., 2013. Radiative Heat Transfer. Academic Press.

NEA, 2012a. OECD-SETH-2 Project PANDA and MISTRA Experiments - Final Summary Report – Investigation of Key Issuesfor the Simulation of Thermalhydraulic Conditions in WaterReactor Containment. Technical Report, Nuclear Energy Agency, https://www.oecd-nea.org/upload/docs/application/pdf/2021-02/csni-r2012-5.pdf.

NEA, 2012b. NEA Publication.

NEA, 2018. Resolving Complex Safety Relevant Issues Related to Hydrogen Release in Nuclear Power Plant Containments Duringa Postulated Severe Accident - Resolving Complex Safety Relevant Issues Related to Hydrogen Release in Nuclear Power Plant Containments During a Postulated Severe Accident. Technical Report, Nuclear Energy Agency.

Nielsen, K.P., Rontu, L., Gleeson, E., 2021. In: Olafsson, H., Bao, J.-W. (Eds.), Uncertainties in Numerical Weather Prediction. Elsevier, pp. 237–264. http://dx.doi.org/10.1016/B978-0-12-815491-5.00009-4.

Paladino, D., Andreani, M., Zboray, R., Dreier, J., 2012. Nucl. Eng. Des. 253, 331–342. http://dx.doi.org/10.1016/j.nucengdes.2011.08.064.

Paladino, D., Dreier, J., 2012. Sci. Technol. Nucl. Instal. http://dx.doi.org/10.1155/2012/239319.

Paranjape, S., Kapulla, R., Fehlmann, M., Suter, S., Bissels, W., Paladino, D., 2018. OECD-NEA/HYMERES-2 project: PANDA test facility description and geometrical specifications. Technical Report TM-41-18-02, Rev-0, HYMERES-2-18-02, Paul Scherrer Institut, Paul Scherrer Institut, 5232 Villigen-PSI, Switzerland.

Piroozmand, P., Mussetti, G., Allegrini, J., Mohammadi, M.H., Akrami, E., Carmeliet, J., 2020. J. Wind Eng. Ind. Aerodyn. 197, 104059. http://dx.doi.org/10.1016/j.jweia.2019.104059.

Rivière, P., Soufiani, A., 2012. Int. J. Heat Mass Transfer 55, 3349–3358.

Saji, G., 2016. Nucl. Eng. Des. 307, 64–76. http://dx.doi.org/10.1016/j.nucengdes.2016.01.039.

Sich, A.R., 2021. In: Greenspan, E. (Ed.), Encyclopedia of Nuclear Energy. Elsevier, Oxford, pp. 30–52. http://dx.doi.org/10.1016/B978-0-12-819725-7.00080-5.

Skillman, G.R., Rempe, J.L., 2021. In: Greenspan, E. (Ed.), Encyclopedia of Nuclear Energy. Elsevier, Oxford, pp. 17–29. http://dx.doi.org/10.1016/B978-0-12-409548-9.12146-3.

Smith, T.F., Shen, Z.F., Friedman, J.N., 1982. J. Heat Transfer 104 (4), 602–608. http://dx.doi.org/10.1115/1.3245174.

Steinhauser, G., Brandl, A., Johnson, T.E., 2014. Sci. Total Environ. 470–471, 800–817. http://dx.doi.org/10.1016/j.scitotenv.2013.10.029.

Tessé, L., Dupoirieux, F., Taine, J., 2004. Int. J. Heat Mass Transfer 47 (3), 555–572.

Unterberger, V., Lichtenegger, K., Kaisermayer, V., Gölles, M., Horn, M., 2021. Appl. Energy 293, 116891. http://dx.doi.org/10.1016/j.apenergy.2021.116891.

Vijaya Kumar, G., Kampili, M., Kelm, S., Arul Prakash, K., Allelein, H.-J., 2020. Nucl. Eng. Des. 365, 110682. http://dx.doi.org/10.1016/j.nucengdes.2020.110682.

Vincenti, W.G., Traugott, S.C., 1971. Annu. Rev. Fluid Mech. 3 (1), 89–116. http://dx.doi.org/10.1146/annurev.fl.03.010171.000513.

Visser, D., Siccama, N., Jayaraju, S., Komen, E., 2014. Nucl. Eng. Des. 278, 491–502. http://dx.doi.org/10.1016/j.nucengdes.2014.08.005.

Wang, P., Fan, F., Li, Q., 2014. Case Stud. Therm. Eng. 3, 51–58. http://dx.doi.org/10.1016/j.csite.2014.03.003.

Wang, L., Yan, B., 2021. Ann. Nucl. Energy 161, 108440. http://dx.doi.org/10.1016/j.anucene.2021.108440.

Wilcox, D.C., 2006. Turbulence Modelling with CFD. D C W Industries.

Xu, G., Li, J., Shi, Y., Feng, X., Zhang, Y., 2022. Urban Climate 45, 101247. http://dx.doi.org/10.1016/j.uclim.2022.101247.

Zhang, J., Li, T., Ström, H., Løvås, T., 2022. Combust. Flame 238, 111876.

Zhang, H., Modest, M.F., 2002. J. Quant. Spectrosc. Radiat. Transfer 73 (6), 649–653.